RESEARCH ARTICLE

Energy

Energy & Environmental Materials WILEY

Quenched PVDF/PMMA Porous Matrix for Triboelectric Energy Harvesting and Sensing

*Assem Mubarak, Bayandy Sarsembayev, Yerzhigit Serik, Abdirakhman Onabek, Zhanat Kappassov, Zhumabay Bakenov, Kazuyoshi Tsuchiya, and Gulnur Kalimuldina**

The rapid development of nanotechnology has significantly revolutionized wearable electronics and expanded their functionality. Through introducing innovative solutions for energy harvesting and autonomous sensing, this research presents a cost-effective strategy to enhance the performance of triboelectric nanogenerators (TENGs). The TENG was fabricated from polyvinylidene fluoride (PVDF) and *N*, *N*′-poly(methyl methacrylate) (PMMA) blend with a porous structure via a novel optimized quenching method. The developed approach results in a high β-phase content (85.7%) PVDF/3wt.%PMMA porous blend, known for its superior piezoelectric properties. PVDF/3wt.%PMMA modified porous TENG demonstrates remarkable electrical output, with a dielectric constant of 40 and an open-circuit voltage of approximately 600 V. The porous matrix notably increases durability, enduring over 36 000 operational cycles without performance degradation. Moreover, practical applications were explored in this research, including powering LEDs and pacemakers with a maximum power output of 750 mW m^{-2}. Also, TENG served as a self-powered tactile sensor for robotic applications in various temperature conditions. The work highlights the potential of the PVDF/PMMA porous blend to utilize the next-generation self-powered sensors and power small electronic devices.

1. Introduction

The revolution in nanotechnology has dramatically influenced the creation of wearable and flexible electronics, opening new paths for the practical application of energy harvesting[1] and autonomous sensors.[2] Integrating triboelectric nanogenerators (TENGs) into wearable devices significantly affects the development of self-powered systems.[3] For instance, TENGs can efficiently convert mechanical energy from routine human motions into electrical power, marking a significant step toward sustainable energy solutions and independent sensor operation.[4] These advancements enable sensors to function without the need for bulky, rigid batteries that demand frequent replacements or recharging.[5] TENGs can transform mechanical movements into electrical energy through friction and electrostatic induction.[6] This technique provides a realistic approach for powering the next-generation wearable electronics and sensors, with applications ranging from continuous health monitoring[7] to environmental sensing.[8] Such applications align with the Internet of Things (IoTs) aims, demonstrating the seamless integration of TENGs into larger technological ecosystems.[9] However, the ability of these devices to efficiently capture and utilize mechanical energy depends on the proper selection of materials.[10] The optimization of materials for better flexibility, stretchability, and energy conversion efficiency can ensure their autonomous functionality and operational efficiency.[11]

Polyvinylidene fluoride (PVDF) has recently gained enormous attention as an alternative flexible piezoelectric polymer to commercial crystalline piezo materials (lead zirconate titanate, quartz, barium titanate, zinc oxide [ZnO], etc.) to generate electricity under the applied force.[12] Polyvinylidene fluoride polymer has five different structural forms (α, β, γ, δ, ε). However, only one delivers piezo responses under deformations. The β-phase of PVDF stands out for being exceptionally efficient at converting mechanical pressure into electrical energy, making it perfect for use in devices that harvest energy from physical movements, like piezoelectric nanogenerators (PENGs)[13] and TENGs.[14] The biggest challenge is achieving a cost-effective methodology for creating oriented β-phase formation in PVDF molecules (H, C, F).[15] Traditional methods for inducing the β-phase in PVDF include heating the material to high temperatures (thermal annealing),[16] electrospinning,[17] mechanical stretching,[18] or applying high electric

A. Mubarak, Dr. B. Sarsembayev, Y. Serik, Prof. G. Kalimuldina
Department of Mechanical and Aerospace Engineering, School of Engineering and Digital Sciences, Nazarbayev University, Kabanbay Batyr Ave. 53, Astana 010000, Kazakhstan
E-mail: gkalimuldina@nu.edu.kz
A. Onabek, Prof. Z. Kappassov
Institute of Smart Systems and Artificial Intelligence, Nazarbayev University, Kabanbay Batyr Ave. 53, Astana 010000, Kazakhstan
Department of Robotics Engineering, School of Engineering and Digital Sciences, Nazarbayev University, Kabanbay Batyr Ave. 53, Astana 010000, Kazakhstan
Prof. Z. Bakenov
Department of Chemical and Materials Engineering, School of Engineering and Digital Sciences, Nazarbayev University, Kabanbay Batyr Ave. 53, Astana 010000, Kazakhstan
Prof. K. Tsuchiya
Micro/Nano Technology Center, Tokai University, 4-1-1 Kitakaname, Hiratsuka, Kanagawa 259-1292, Japan
The ORCID identification number(s) for the author(s) of this article can be found under https://doi.org/10.1002/eem2.12808.

DOI: 10.1002/eem2.12808

fields.[19] Although these techniques are effective, they are energy and labor-intensive, requiring specialized and expensive equipment. Moreover, during mechanical stretching, the degree of stretching must be carefully considered[18] to avoid material deformation. In the case of electrospinning,[17,19] precise control over various parameters is necessary to obtain more stable fiber mats for nanogenerators. In contrast to the known conventional manufacturing techniques, we propose developing a simple quenching method without additional postprocessing steps to achieve highly polarized β-phase PVDF flexible films.[20] Oka and Koizumi[21] first described the quenching mechanism by presenting the formation of the β-phase form of PVDF based on nucleation and growth theories and proved the effectiveness of low-temperature quenching. The straightforward approach provides a high cooling rate that effectively induces high β-phase content by locking polymer chains in extended polymer conformation.[22] Considering the results of the above studies, we set the task of attaining high β-phase content in PVDF by quenching at extremely low temperatures.

Although the method could be considered simple and efficient, the rapid crystallization during the quenching can result in a nonuniform distribution of crystalline and amorphous regions within the PVDF structure.[22] The results in the previous studies[20,23,24] have also reported the formation of a β-phase fraction under certain optimal conditions based on choice of solvents, centrifugation speed, and quenching bath temperature.[25] Therefore, we considered integrating PVDF with other additives that facilitate appropriate nucleation and crystallization toward the coveted β-phase.[26,27] The strategic incorporation of certain additives strengthens PVDF's thermal and mechanical properties, making it susceptible to quenching and increasing its triboelectric effectiveness.[28] In this context, materials, such as carbon nanotubes,[29] N, N′-poly(methyl methacrylate) (PMMA),[26,27,30] polyaniline,[25] and ZnO,[31] have been synergized with PVDF. PMMA appears especially favorable because of its low mass density and considerable aspect ratio, which increase PVDF's mechanical, thermal, and electrical properties.[32,33] More importantly, the amorphous structure of PMMA acts as a barrier to prevent PVDF from quickly forming its crystals during quenching.[27] This slow-down in crystallization helps produce more of the β-phase PVDF crystals. However, the traditional methods used to incorporate PMMA and other additives into PVDF, such as creating flat, stacked layers,[22] or thin films[16] through spin-coating and casting, have limitations as small-scale contact areas. This limitation can restrict the full capacity of TENG's electrical and mechanical properties, leading to suboptimal electricity generation from the mechanical movements or forces applied.[34] TENGs based on porous materials have superior properties such as thermal resistance and electromagnetic interference shielding[35] and can be used for numerous applications, including harvesting systems and sensing. Therefore, it is essential to construct high-performance TENGs based on high surface area PVDF using the quenching method to promote the widespread application and commercialization of TENGs. Considering previous studies, in this work, the novelty lies in forming highly desired β-phase stabilization in the PVDF porous matrix with high surface area by quenching with liquid nitrogen in an ice bath and blending with PMMA.

Furthermore, this study focused on a TENG device based on a PVDF/PMMA blend porous matrix to demonstrate its potential in energy harvesting and self-powered sensing applications. The effective combination of an ice bath and liquid nitrogen quenching achieved a high β-phase of 85.7% in the PVDF-based porous matrix. Operating at a constant applied force of 10 N, the PVDF/3wt.%PMMA blend porous TENG produced a voltage of 600 V and a short-circuit current of 1.2 μA. The maximum power output is 750 mW m^{-2}, demonstrating the competitiveness of the prepared TENG design in energy harvesting applications. Furthermore, PVDF/3wt.%PMMA porous TENG was further tested as self-powered tactile sensors operating in various temperatures, showcasing the high stability of the sensor in robotic gripper manipulations.

2. Results and Discussion

2.1. Materials and Electrical Characterizations

Crystalline modification of the as-prepared PVDF films fabricated at various processing conditions was investigated using FT-IR spectroscopy, and the results are presented in **Figure 1**a–d. To determine the optimal quenching conditions for the β-phase transformation of PVDF films, 20 wt.% PVDF solution is divided into three parts for posttreatment: liquid nitrogen quenching, ice bath with liquid nitrogen quenching, and slow cooling, the last of which was a control experiment. The samples displayed the piezoelectric β-phase, confirmed by absorption bands at 1280 and 840 cm^{-1}. As seen in Figure 1a, the slow cooling procedure does not significantly influence the crystallization of PVDF. The value F(β) 55.6% calculated via Equation (2) remains low for samples, as highlighted in Figure 1b. The bands of α-phase of PVDF at 763, 795, 853, and 975 cm^{-1} were observed on the infrared spectrum of PVDF films. There is no noticeable increase in F(β) 59.8% even with introducing a liquid nitrogen quenching method. However, when the ice bath and liquid nitrogen were combined, the F(β) for samples increased to 73.2%, indicating the superiority of such combined quenching to achieve the β-phase transformation in PVDF films. This method was further selected to blend PVDF with PMMA, where PMMA was added to attain uniform crystallization and formation of the desired β-phase. For instance, De Neef et al.[26] studied crystallization kinetics and provided insight into the mechanism of how PMMA retards the crystallization of PVDF. The key findings of this study are the reduction in cooling rate required for β-phase formation in the presence of PMMA, lower crystallization temperatures, and enthalpies. Moreover, PMMA effectively improves the nucleation and growth of PVDF crystals.[22] The studies effectively demonstrate that PMMA acts as a nucleation inhibitor for the α-phase, promoting the β-phase and thus altering the crystallization kinetics during quenching.

As a result, the content of the β-phase of PVDF changed sharply with the addition of PMMA. We can observe the β-phase peak increases with the PMMA content from 1 to 3 wt.%. However, this trend slows when the PMMA concentration reaches 5 wt.% (Figure 1c). The FT-IR results show PVDF with 3 wt.% PMMA achieved extremely high β-phase transition through ice bath quenching with liquid nitrogen, resulting in 84.5% (Figure 1d). The addition of PMMA could facilitate α-phase transformation into polar β-phase in PVDF. According to Xia and his colleagues,[19] this might be due to the formation of hydrogen bonding between the O atom in the carbonyl groups of PMMA and the H atom in the CH_2 groups of PVDF. The band at 1280 cm^{-1} belongs to the CF_2 groups in PVDF, and the peaks at 1151 and 1256 cm^{-1} confirm the presence of C–O–C bonds in PMMA. Mixing PMMA in a small amount caused structural changes in PVDF, aligning its molecules in an all-trans structure, which promotes primary crystallization in the β-

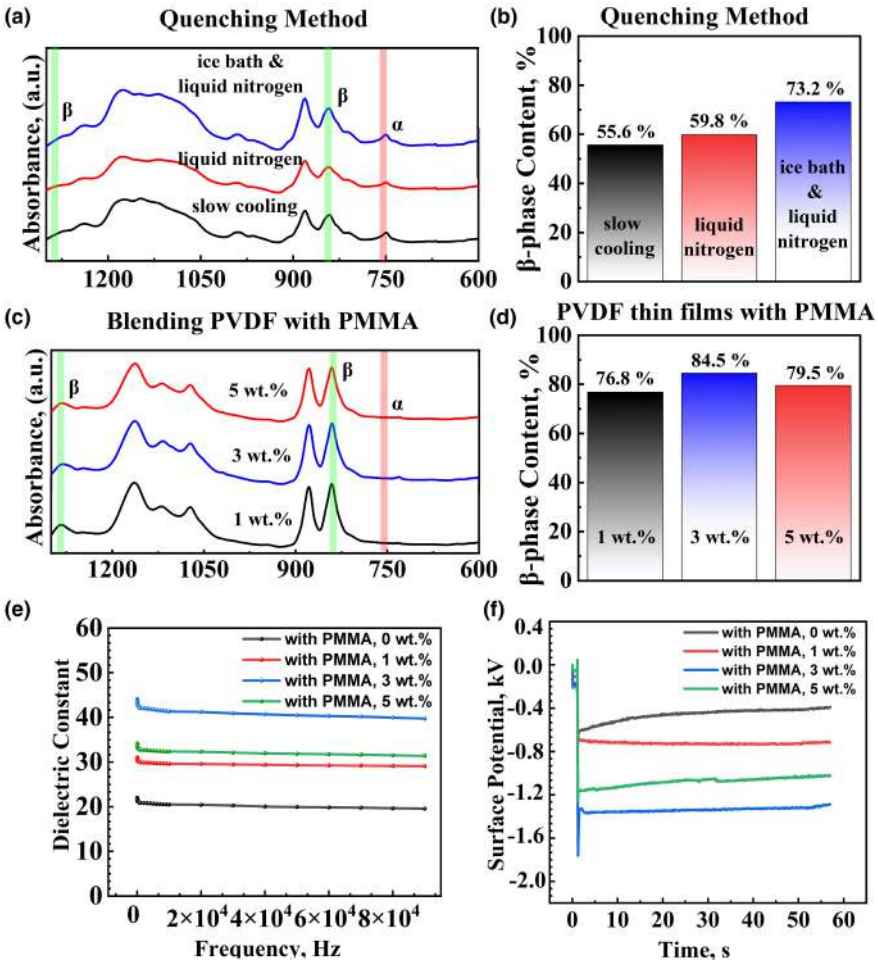

Figure 1. FT-IR spectra analysis of a) pristine PVDF quenching methods, b) β-phase content of pristine PVDF, c) blending PVDF with PMMA and quenched via ice bath and liquid nitrogen, d) β-phase of PVDF/PMMA, dielectric properties of the PVDF-based films with various PMMA content: e) dielectric constant, f) surface potentials. PMMA, *N, N′*-poly(methyl *methacrylate); PVDF, polyvinylidene fluoride.*

phase. These results suggest hydrogen bonds promote molecular interactions and structural modifications in PVDF/PMMA blends, as previously reported in the literature.[26,32,33]

Furthermore, XRD analysis was carried out to reconfirm the crystal structure and composition of the PVDF in F(β) content calculations (Figure S1, Supporting Information). The X-ray diffraction (XRD) patterns of the PVDF films crystallized from various quenching methods exhibit unique peaks at 20.7 and 41.2°, characteristic of the β-phase in PVDF.[36,37] As shown in Figure S1a, PVDF prepared by slow cooling had prominent diffraction peaks at 18.11°, 19.73°, and 26.35°, regarded as a nonpolar α-phase.[15] After PVDF films were quenched with an ice bath and liquid nitrogen, the intensity and position of the PVDF diffraction peak were reduced and shifted due to recrystallization. Quenching altered the strength and location of the PVDF diffraction peak. As a result, the α-phase diffraction peaks either reduced in intensity or disappeared at 18.11° and 26.35°. Moreover, the α-phase diffraction peak moved to a lower angle at 19.73°, creating a new diffraction peak of the β-phase (110) (200) at 20.7°.[38] This shift and a new peak at 20.7° signify the formation of the electroactive β-phase to the original α-phase.

Additionally, it was found that introducing 3 wt.% PMMA to the PVDF films not only shifted the diffraction peaks but also eliminated the α-phase, facilitating a more pronounced β-phase presence (Figure S1b). The content of β-phase reached 84% according to calculations via Equation (3), which verified the feasibility of the ice bath and liquid nitrogen quenching method. The analyzed XRD patterns of the PVDF/PMMA samples were consistent with the FT-IR β-phase content calculations.

Figure 1e illustrates the dielectric constants for pure PVDF and its blends with PMMA at varied wt.%. Dielectric samples were strategically placed between two electrodes and tested over the specified frequency range (20–80 kHz) to measure the capacitance and dissipation factor. The baseline pristine PVDF exhibited a dielectric constant that started at 22 at the lower frequency of 20 Hz. As the frequency increased, there was a slight decrease in the constant, reaching 19.6, and this value became stable from 50 kHz onward, irrespective of further frequency increments. Polyvinylidene fluoride with 1 wt.% of PMMA resulted in an appreciable enhancement in the dielectric constant. It initiated at a significantly higher value of 31.2 at 20 kHz, and as the frequency escalated, the value tapered off, settling at 29.4 for higher frequency ranges. A prominent shift was observed when the PMMA content was increased to 3 wt.%. The dielectric constant reached 44 at 20 kHz. After this initial spike, it stabilized, converging to 40 at 50 kHz. However, at 5 wt.% PMMA, the dielectric constant started at 34.5 at the lowest frequency (20 Hz), then experienced a decline to 32.5 by 50 kHz, and finally, the value plateaued at 31.5 for the higher frequencies. Therefore, the optimal concentration of PMMA can improve the dielectric properties of PVDF material.

Furthermore, Figure 1f demonstrates the surface potential measurements over time for the PVDF/PMMA blends with various concentrations. Notably, after undergoing the process of triboelectrification, the surface potential for this blend surged remarkably. Specifically, the PVDF/3wt.%PMMA showcased a value that was 3.5 times that of pristine PVDF, attaining a lower −1.35 kV compared to the −0.37 kV of the pure PVDF film, all within a short time frame of 60 s. As highlighted in Figure 1f, a takeaway from this observation is the intrinsically negative surface potential of PVDF-based films, which emphasizes their predominant tribo-negative nature. This phenomenon is related to the many highly electronegative fluorocarbon segments in PVDF. According to research by Lolla et al.[39]and Wang et al.,[36] when a PVDF membrane is subjected to a high electrical voltage, numerous dipoles within the material are polarized. The dipoles become aligned in a specific direction, significantly enhancing the variation in the surface potential of the polymer. We can conclude from the dielectric constant and surface potential studies that PVDF/3wt.%PMMA films are the most prominent samples for further structural modifications.

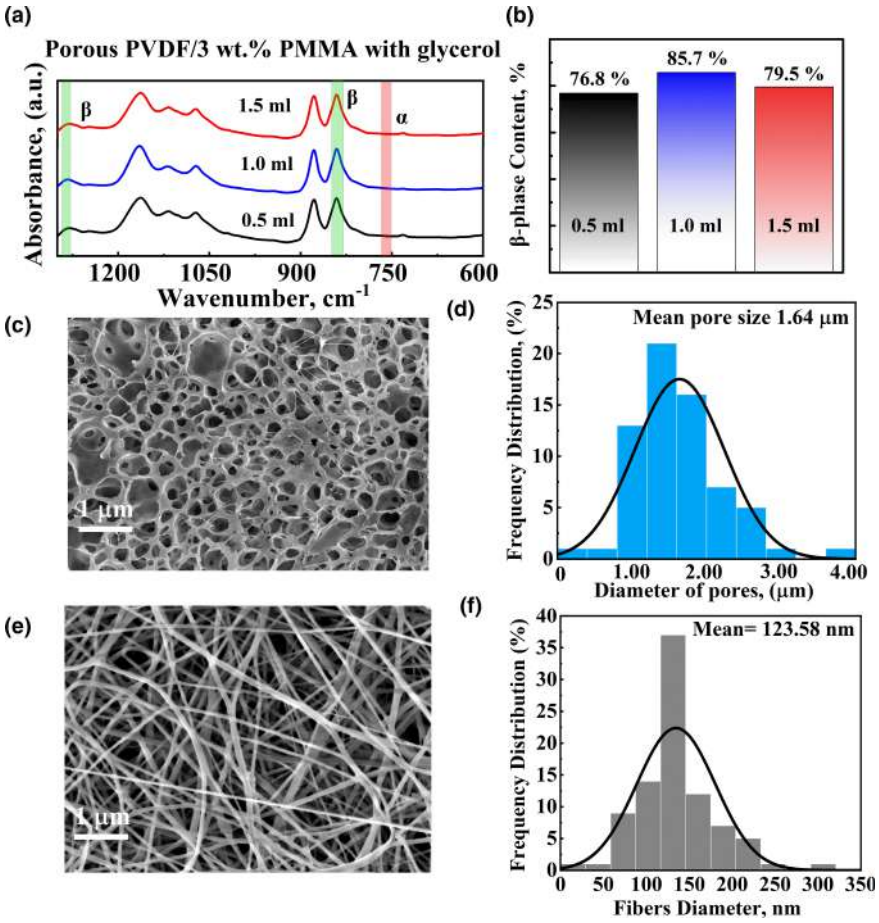

Figure 2. a) FT-IR spectra analysis and b) β-phase content of PVDF/3wt.%PMMA porous matrix, SEM morphology analysis of layer for two electrodes of TENG: c) tribo-negative porous PVDF/3wt.%PMMA porous matrix, d) and pore distribution analysis e) tribo-positive Nylon-6 fibers via electrospinning, and f) fiber distribution analysis.

Therefore, the PVDF/3wt.%PMMA porous matrix was prepared by adding glycerol from 0.5 to 1.5 ml in different volumes. To define the influence of the porous agent on the β-phase content, analyses were carried out via FT-IR (**Figure 2a**) and XRD (Figure S1, Supporting Information) techniques. As depicted in Figure 2a, adding various volumes of glycerol (0.5–1.5 mL) to these samples did not significantly impact the purity of the material. However, adding 0.5 mL of glycerol decreased the absorption peak to 840 cm^{-1}, which affects F(β) to reduce to 76.8%. Although 1.5 mL did not significantly affect F(β) of PVDF/3wt.%PMMA, the solution is separated into two phases due to DMF and glycerol density differences during the synthesis. As depicted in Figure 2b, adding 1 mL of glycerol to PVDF/3wt.%PMMA did not reduce F(β), and the β-phase content remained impressively high at 85.7%. Therefore, this volume was introduced into the PVDF/3wt.% PMMA matrix to increase the surface contact area of the triboelectric layer.

Then, the highest β-phase content PVDF/3wt.%PMMA porous matrix morphology was studied via SEM analysis (Figure 2c), demonstrating pronounced uniformity in pore distribution throughout the material. This increased porosity and the inherent significant area-to-volume characteristic amplify the contact area, which is critical for its intended applications.[40] Figure 2d presents that the mean pore size is approximately 1.64 μm, with a majority (over 60%) ranging between 1 and 2 μm in diameter. As a tribo-positive layer, Nylon-6 fibers were fabricated via electrospinning with an SEM image of the morphology demonstrated in Figure 2e. We can observe fibrous bead-free structures with an average fiber diameter of 123.58 nm, as depicted in Figure 2f. Notably, approximately 40% of all fibers possessed similar diameters, around 125 nm, aligning with the optimal electrospinning conditions.

The study further investigated the effect of PMMA blending with PVDF and the fabrication of porous matrices on the triboelectric effect for TENG applications. In **Figure 3a**, we can observe the TENG structure consisting of PVDF-based mats, serving as the negative triboelectric layers, were paired with Nylon-6 fibers, which functioned as the positive triboelectric layer. This combination facilitated the construction of vertical contact-separation mode TENG. Under a consistently fixed working condition—characterized by an impact force of 10 N and a working frequency of 5 Hz—the triboelectric outputs were recorded and analyzed. As shown in Figure 3b,c, the triboelectric output of PVDF/PMMA (PMMA = 0, 1, 3, 5 wt.%) based TENGs were first analyzed to optimize the concentration of PMMA.

Initially, to confirm the existence of piezo responses in the high β-phase content PVDF/PMMA films, PENGs were fabricated using Cu tapes on both sides of the prepared films. The results are demonstrated in Figure S2, Supporting Information, with excellent piezoelectric output of the prepared films, where the highest voltage was observed in PVDF/3wt.%PMMA at 16.5 V with four times higher voltage than that of pure PVDF. Therefore, we expected a similar trend when applied to TENG performance characteristics with PVDF/PMMA blend films, further confirmed in Figure 3.

In the TENG configuration testings, when the concentration of PMMA increased from 0 to 1 wt.%, the output voltage of the PVDF/PMMA blend film with Nylon-6 fibers TENGs gradually increased from ~85 to ~91 V (Figure 3b). At the same time, the corresponding short-circuit current increases from ~0.4 to 0.7 μA (Figure 3c). Further increase of PMMA content to 3 wt.% results in higher voltage and short-circuit current output as ~114 V and ~0.9 μA, respectively. Meanwhile, when 5 wt.% of PMMA was added, a decreasing trend to around 100 V was observed. Jain et al.[16] previously studied a similar trend in a mixture of semi-crystalline and amorphous polymers, where a high concentration of PMMA causes phase separation, resulting in the formation of three phases: PVDF crystallites, a crystalline amorphous PVDF interfacial phase, and a mixed amorphous PVDF/PMMA phase. The phase separation could be one of the reasons for the lower output of higher than 3 wt.% PMMA blend in PVDF films. From the piezoelectric and triboelectric properties, we can

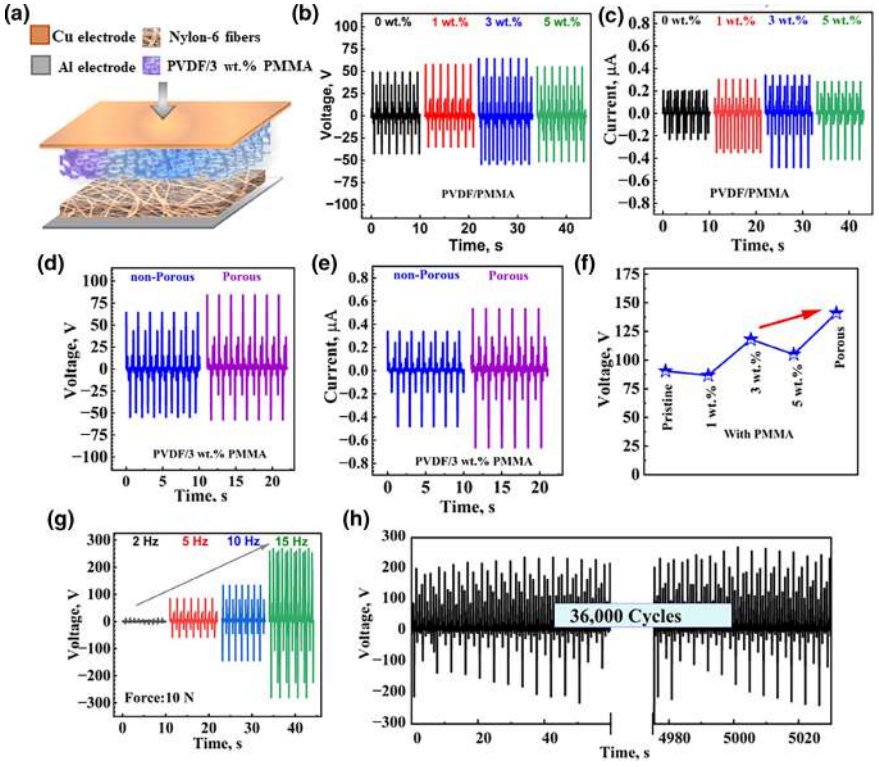

Figure 3. The performance of PVDF-based TENGs under 10 N and 5 Hz: a) schematic illustration of TENG, b) open-circuit voltage and c) short-circuit current of blending PVDF with PMMA, d) open-circuit voltage and e) short-circuit current of nonporous and porous PVDF/3wt.%PMMA TENG, f) summary of highest voltage output, g) output voltage in various frequencies, and h) durability test for 36 000 compressions of porous PVDF/3wt.%PMMA TENG. PMMA, *N, N′*-poly(methyl *methacrylate); PVDF, polyvinylidene fluoride; TENG, triboelectric nanogenerators.*

define that PVDF/3wt.%PMMA exhibited the highest voltage and short-circuit current due to the enhanced dielectric properties (Figure 1e) and high surface potential (Figure 1f) of the films achieved via ice bath and nitrogen quenching.

As a next step, to define the role of a porous matrix in triboelectrification, comparisons were drawn between the performances of nonporous and porous PVDF/3wt.%PMMA TENGs under the same testing conditions. Figure 3d demonstrates the superiority of the porous matrix, where the output voltage was heightened by 1.3 times, reaching 140 V, compared to the nonporous PVDF-based TENG. Moreover, a similar trend was consistently observed in short-circuit current measurements, where the porous matrix elevated the output by more than 1.5 times, registering 1.2 μA (Figure 3e). The TENG designed with a porous PVDF/3wt.%PMMA matrix records a voltage 25 V higher than the PVDF/3wt.%PMMA film structure (Figure 3f). In contrast to other techniques that struggle to create and maintain gaps between two layers, porous structures naturally generate opposing charges and currents when compressed.[41] Porous dielectrics contain air gaps, simplifying the design and improving the efficiency and durability of TENGs.[42] Therefore, TENG based on a porous PVDF/PMMA matrix was considered for further characterization.

As a promising power source for electronic devices, evaluating the triboelectric performance of PVDF/PMMA porous TENGs under different operating conditions is necessary. Thus, the relationship between the triboelectric output of this TENG and controllable operation parameters with varying frequencies was investigated. A linear motor, operating at a consistent impact force of 10 N, was employed for this purpose, and the outcomes are illustrated in Figure 3g. The observations denote a linear relationship between output voltage and input frequency. Although the increase in open circuit voltage does not directly depend on frequency, it can be explained by the rise in pressure with increasing frequency and the accumulation of surface charge.[43] High pressure increases contact surface area due to more significant deformation of the porous matrix. Moreover, the higher contact frequency prevents natural charge neutralization and thus promotes surface charge accumulation.[41] As the frequency escalated, so did the PVDF/3wt.%PMMA output voltage, demonstrating a direct proportionality. Remarkably, at 15 Hz, the output voltage reached 600 V, which is higher than the voltage observed at the baseline frequency of 2 Hz.

As a sustainable power source for electronic devices, the high stability and reliability of TENG are indispensable. Thus, the stability of a $35 \times 35\ mm^2$ PVDF/3wt.%PMMA porous TENG was first assessed by operating it at a contact frequency of 15 Hz for over 36 000 cycles, with the corresponding triboelectric output shown in Figure 3h. Within the experiment, no noticeable changes in the output voltage and current were observed, suggesting the excellent durability of porous TENGs.

2.2. Energy Harvesting and Tactile Sensing Applications

This section discusses the mechanical energy harvesting capability to power small electronics and self-powered sensor applications in detail. Despite its ability to reach high open-circuit voltages up to hundreds of volts, TENG's power output is usually meager due to the high output impedance and low charge transfer.

The power density curve of the TENG with optimal PVDF/3 wt.% PMMA porous matrix was calculated using Equation (1):[42]

$$P_{density} = \frac{(I_{rms})^2 R_l}{A} \quad (1)$$

where I_{rms} is the measured current, R_l is the load resistance, and A is the TENG's size. According to Equation (1), a peak point at $750\ mW\ m^{-2}$ across a matching impedance of the source at 87 MΩ is presented in **Figure 4**a. The measured currents and estimated voltage responses across ranging resistors connected to TENG's power converter circuit as external loads are given next (Figure 4b). A full-wave bridge rectifier circuit was used to

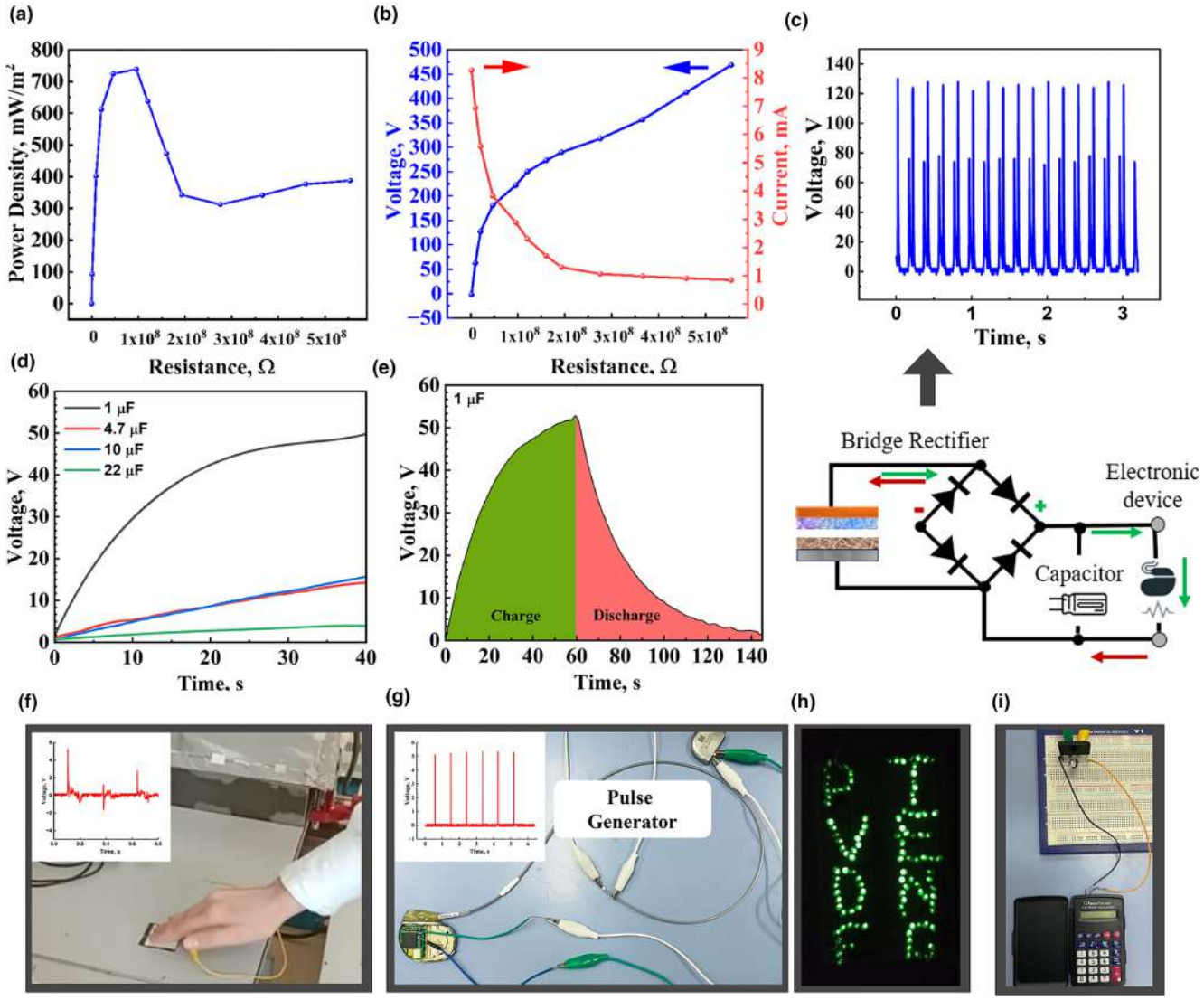

Figure 4. a) Output power density, b) the current and voltage with variable load resistors, c) a rectified output voltage, d) the charging curves of 1, 4.7, 10, and 22 μF capacitors, e) the charge–discharge time of 1 μF capacitor, f) the responses of hand-tapping, g) the powering of the pulse generator, h) the lighting of 116 LEDs, and i) the powering of the calculators.

convert the power from AC to DC harvested by TENG (Figure 4c). The generated power by the TENG cannot be fed to small electronics due to voltage rate requirements. Therefore, energy storage devices such as capacitors or small batteries should be used.

We have charged 1, 4.7, 10, and 22 μF capacitors under 15 Hz and 35 N to 50, 16, 14, and 5 V within 40 s by the champion PVDF/3wt.%PMMA porous TENG, respectively (Figure 4d). The charging rates of the capacitors are calculated as 1.25 V/sec@1 μF, 0.35 V/sec@4.7 μF, 0.4 V/sec@10 μF, and 0.125 V/sec@22 μF, respectively. Furthermore, the 1 μF is charged up to 52 V within 58 sec then left for self-discharging for 87 s (Figure 4e). The findings above demonstrate that the PVDF/3wt.%PMMA porous TENG has a high charging rate that can power various small electronic devices.

The single-electrode mode testing with hand tapping was demonstrated in Figure 4f (Video S1, Supporting Information). Furthermore, applying TENG to power implantable devices from biomechanical motions has become a new trend. Therefore, we considered driving a cardiac pacemaker with energy generated by the TENG. The cardiac pacemaker with the removed battery created pulses driven by energy accumulated in a 1 mF capacitor charged by the TENG up to 3 V within 2.75 h (Figure 4g and Video S2, Supporting Information). Also, we tested the performance of the TENG by lightning 116 LEDs connected in series (Figure 4h and Video S3, Supporting Information). Finally, the 220 μF capacitor was charged to 2 V, sufficient to drive the calculator (Figure 4i and Video S4, Supporting Information). The demonstrated results confirm the feasibility of powering the real-life applications by PVDF/3wt.%PMMA porous TENG and the future practical implementation for small electronics in medicine and IoTs.

The comparative analysis of output performances for various PVDF-based TENGs, as outlined in **Table 1**, reveals that the PVDF/3 wt.%

Table 1. Comparison of PVDF-based TENG performances.

Material	Preparation method	F(β), %	Morphology	Output voltage	Power density	Durability	References
PVDF/PMMA	Annealing	78.0	Flat film	—	—	—	[16]
$BaTiO_3$ /PVDF	Mechanical stretching	—	Thin film	130 V	—	—	[18]
PVDF/Cellulose	Solution-casting	—	Thin film	410 V	0.136 mW cm^{-2}	—	[9]
PVDF/PMMA	Electrospinning	83.9	Fiber mat	190 V	13.8 W m^{-2}	10 000 cycles	[19]
PVDF/ZnO	Solution-casting	92.0	Thin film	185 V	338 μW cm^{-2}	—	[31]
PVDF/3 wt.% PMMA	Ice bath/liquid nitrogen quenching	85.7	Porous matrix	600 V	750 mW m^{-2}	36 000 cycles	This work

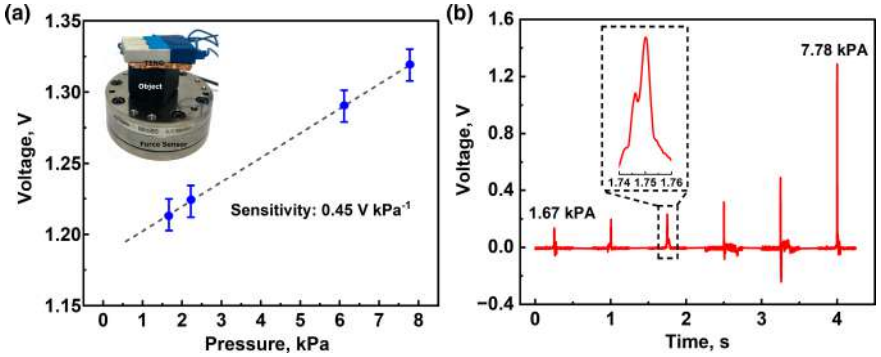

Figure 5. a) The sensitivity curve of a PVDF/3wt.%PMMA TENG-based tactile sensor under various pressures and the corresponding test bench with an industrial force torque sensor. b) The sensor responds to a wide range of pressure.

PMMA TENG exhibits a higher maximum power density than other studies.[31] This suggests an enhancement in the electrical properties of PVDF when blended with PMMA, alongside applying an optimal quenching method. Notably, the open circuit voltage output of the PVDF/3wt.%PMMA TENG, which reaches 600 V, is significantly greater than observed in other techniques, which range between 130–410 V.[9,18,19,31] The results further validate that developing porous PVDF/3wt.%PMMA matrix ensures the high durability of the TENG, making them suitable for high-performance energy harvesting systems.

Moreover, PVDF/3wt.%PMMA TENG can be used as a sensor to measure the degree of applied external force. The sensor sensitivity measurement circuit shown in **Figure 5**a consists of a TENG, a Nylon object, and an industrial pressure sensor. The data were measured several times for each applied force to create a calibration curve. In past studies,[35,44–46] the sensitivity of sensors ranged from 0.013 to 0.29 V kPa^{-1}. For comparison, the applied force in the study was converted to pressure using the contact area (30×30 mm^2). The high linear sensitivity of the sensor exhibited 0.45 V kPa^{-1} (Figure 5a) over a wide range of load forces from 15–70 N, corresponding to 1.67–7.78 kPa. Figure 5b demonstrates the voltage characteristic of the sensor with a direct single-contact load at a pressure of 1.67–7.78 kPa, respectively. This clearly shows that the maximum output voltage increases linearly with increasing pressure. Moreover, the response time is highly dependent on the data acquisition system. In this study, the sampling rate of the self-powered TENG tactile sensor system was 100 Hz, resulting in a bandwidth of 50 Hz and a fast response time of about ~10–15 ms.

Then, to showcase the developed TENG's dual functionality as an energy harvester and tactile sensor, we interpreted the electrical charge produced by the TENG as a signal of physical contact. The object was manipulated using 7 degrees of freedom torque-controlled robot arm gripper equipped with porous PVDF/3wt.%PMMA TENG as a tactile sensor. During grasping, this tactile sensor triggers the gripper to handle the grasped object without damaging it. An instrumentation platform with an industrial force–torque sensor was developed to obtain ground-truth force measurements and an array of ceramic power resistors to simulate temperature variations. The power resistors and the self-powered PVDF/3wt.%PMMA porous TENG tactile sensor were attached to one finger of the gripper, while the force-torque sensor was attached to the opposite finger (**Figure 6**a).

An electrical charge surges when the tactile sensor hits a dielectric material, a nylon object. The repetition of the impact force during 10 grasps and signals generated by the sensor are shown in Figure 6a, respectively. During the grasping at 1 s, the commercial force sensor indicates a 70 N force value, then holds for 3.5 s before the release, where the force drops back to the initial value. This process was correlated with the working mechanics of the PVDF/3wt.%PMMA porous TENG tactile sensor in Figure 6b. The sensor and force sensor outputs were sampled at 100 Hz using data acquisition boards integrated into one system using the Robot Operating System (ROS). It was detected that the sensor is sensitive to the rate of change of the applied force, where the output was recorded when the time derivative of the force was maximum. In Figure 6b, during the grasping at about 1 s, we can correlate 70 N applied force to hold the object with the peak value of 200 for the TENG tactile sensor. The self-powered tactile sensor output was detected in terms of peak values. The 10 repetitions of the same manipulation provided accurate and repeated tactile sensor values. This maximum voltage the sensor generates triggers the gripper controller to stop, avoiding the deformation of an object. To further study the self-powered sensor's ability to work at harsh temperature conditions, the power resistors were different levels of DC current to heat the PVDF/3wt.%PMMA porous TENG sensor to 25, 60, and 90 °C. The system also established the force-torque sensor to confirm that the same amplitude of the applied force had been used. Figure 6c depicts the amplitudes of the peak voltages for the three given ambient temperatures. PVDF/3wt.%PMMA porous TENG sensor response voltages rise with the temperature. Xia et al.[14] explained that high temperatures lead to greater polarizability of PVDF and promote the alignment of dipolar molecules with the electric field, thus improving the output of

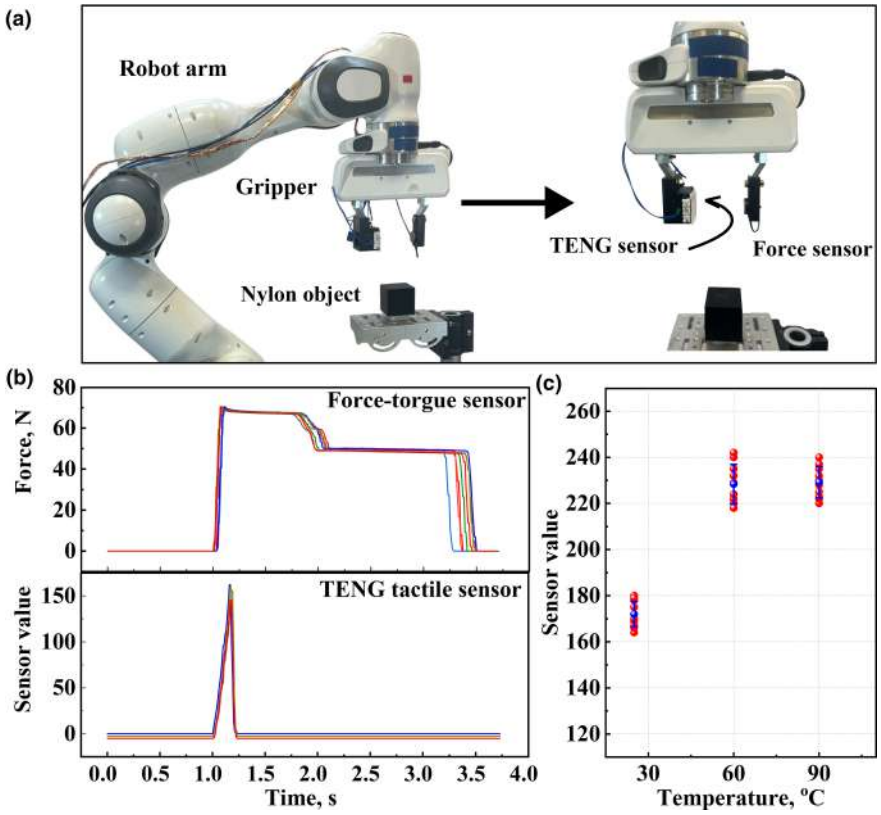

Figure 6. a) Schematic design of an assembled gripper, b) real-time voltage signals measured from the ground-truth force–torque sensor and TENG tactile sensor, including the contact and grasp. c) Grasping the same object with increased temperature (25, 60, 90 °C). TENG, triboelectric nanogenerators.

autonomous sensors. The study confirms that the prepared self-powered tactile sensor responds to the applied force to grasp an object at even elevated temperatures.

3. Conclusion

An approach was successfully demonstrated to increase PVDF/3wt.% PMMA porous matrix performance in the dual application as a TENGs and self-powered tactile sensor. Our work has focused on forming a PVDF matrix by optimizing quenching conditions and blending with PMMA. Finally, we achieved a high β-phase content (85.7%) of PVDF/3wt.%PMMA, leading to the dielectric constant of 40. The effect of the porous structure on the triboelectric properties of the material was also studied by direct comparison with an equivalent PVDF/3wt.% PMMA solid film. The porous matrix demonstrated significantly better mechanical robustness over 36 000 cycles. Additionally, the contact pair of Nylon 6 fibers and the porous PVDF/3wt.%PMMA matrix demonstrated excellent triboelectric performance, suitable for energy harvesting, achieving a voltage of 600 V and peak power of 750 mW m^{-2} at a frequency of 15 Hz. TENG achieved a potential for energy harvesting to power low-energy electronics, including calculators, LEDs, and pacemakers. The sensor capabilities of the PVDF/3wt.%PMMA matrix were also tested using a robotic gripper for object recognition, showcasing its thermal stability and quality as a sensor. Overall, the improved durability and triboelectric properties of the porous PVDF/3wt.%PMMA matrix have significant potential for forming energy harvesting systems and autonomous sensors.

4. Experimental Section/ Methods

Materials: N,N′-dimethylformamide (DMF, ACS reagent, >95.8%), glycerol (≥99.0%), polyvinylidene fluoride (PVDF) pellets with specific Mw ∼ 400 000 g mol^{-1} by GPC, atactic PMMA with Mw ∼ 350 000 by GPC, and Nylon 6 pellets with Mw = 224.30 g mol^{-1} by GPC were provided by Sigma-Aldrich and used without further modification.

Fabrication of PVDF/PMMA blend films: The PVDF 20 wt.% was dissolved in DMF at 40°C under magnetic stirring for 2 h. Three methods were applied to improve the crystalline structure of the polymer for electroactive PVDF preparation. Initially, the optimal conditions for quenching were identified. This was evaluated by comparing cooling methods such as slow cooling, liquid nitrogen quenching, and ice bath quenching with liquid nitrogen. Then, the effect of blending PMMA material in various concentrations between 0 and 5 wt.% was studied to achieve uniform crystallization. Finally, glycerol was added at the ratio between 0.5 and 1.5 ml in 20 ml of the solution by ultrasonication for 20 min at 45°C to achieve a porous matrix (**Figure 7a**). All samples were blade coated in 300 µm thickness on the surface of an Al foil. To completely remove the glycerol, samples were kept in a water bath at 40 °C for 12 h. The last step was drying in an oven at 50 °C for 2 h.

Quantification of β-phase in PVDF: The change in anisotropy, degree of crystallinity, crystalline phase, and other morphological changes that occur during transformation can be identified using various characterization techniques such as XRD, and Fourier transform infrared spectroscopy (FT-IR). The analysis of phase transformations in the PVDF film is discussed below.

Vibrational bands via FT-IR of the α-phase could be defined at 530, 615, 765, and 795 cm^{-1}, while vibrational bands exclusively of the β-phase are 1280 and 840 cm^{-1}. The IR absorption bands, characteristic of the α and β phases in each sample, are at 765 and 840 cm^{-1}. The absorption coefficient at the corresponding wavenumber for each phase (=6.1×10^4 and = 7.7×10^4 cm^2 mol^{-1}). Thus, for a system α and β phases, the relative fraction of β-phase, $F(\beta)$, can be calculated using Equation (2):[47]

$$F(\beta) = \frac{X_\beta}{(X_\alpha + x_\beta)} = \frac{A_\beta}{\left[(k_\alpha/k_\beta)A_\alpha + A_\beta\right]} = \frac{A_\beta}{1.26A_\alpha + A_\beta} \quad (2)$$

where the A_α and A_β are the absorption bands for α and β phases, respectively.

The FT-IR phase calculations were further reconfirmed via XRD analysis. The peaks corresponding to the 2θ values of 17.7°, 18.4°, and 19.9° are defined as characteristic of the α-phase. The peak at 20.7° is due to the sum of the diffraction in the (110) and (200) planes, which is a characteristic of the β-phase and can be defined in Equation (3):[48]

$$\frac{X_\beta}{X_\alpha} = k\frac{I_\beta}{I_\alpha} \quad (3)$$

where X_α is the weight fraction of the amorphous phase, and X_β that of the crystalline phase (i.e., the crystallinity), I_α and I_β are the diffraction peak

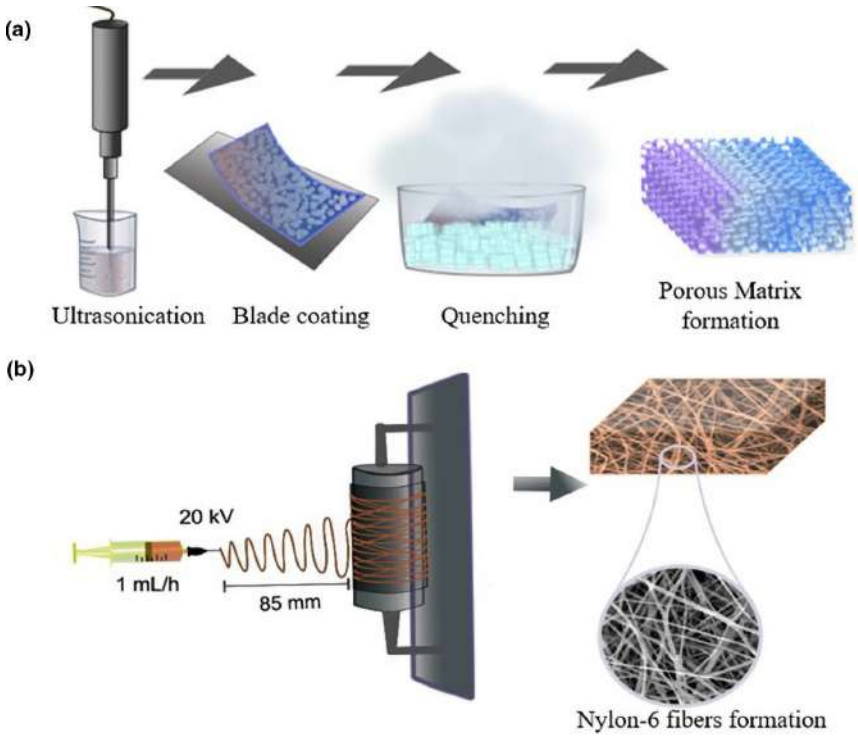

Figure 7. a) Fabrication of tribo-negative PVDF/PMMA porous matrix via liquid nitrogen in ice bath quenching and b) tribo-positive Nylon-6 fibers mat preparation via electrospinning.

intensity. XRD spectra were collected at 2θ from 5° to 45° and X_α, X_β were obtained through the summation of the integrated area under the bump peak over the total summation of the integrated area under both crystallinity β-phase and amorphous α-phase[29].

Nylon fibers via electrospinning: Nylon-6 fibers (tribo-positive layer of TENG) were prepared using a 15 wt.% solution of Nylon-6 in formic acid (CH_2O_2). The setup consisted of a flat collector positioned 85 mm from the needle tip, and the electrospinning was carried out at room temperature with a controlled humidity of 22%. A flow rate of 1 mL h^{-1} and an applied voltage of 20 kV was used to achieve the spinning. The fibers were collected on the Al foil flat collector, and the residual solvent evaporated at room temperature (Figure 7b).

Preparation of TENG device and self-powered tactile sensor: The tribo-negative layer from PVDF-based films was stuck with Cu tape as an induction electrode in size 35 × 35 mm^2. The tribo-positive layer of the Nylon-6 fibers was collected in Al tape of the same size. TENG operates based on the contact-separation mode with an initial fixed distance of 5 mm between two dielectric materials. Spacers were added between the tribo-positive and tribo-negative layers to optimize the design. These spacers were placed along the parallel edges of the layers, ensuring that the dielectric materials made full contact with each other. A motorized force and torque tester provide mechanical strain to test the constructed TENG with two electrode layers against a calibrated compressive force. The linear motor (LinMot P01-37 × 120/80 × 160) is used to implement the contact-separation mode of the TENG working under various frequencies. Thedual-range force sensor (Vernier, ±50 N) was used to measure the applied force on the surface of the TENG.

The tactile sensor made from the best sample PVDF/3 wt.% PMMA porous TENG was used to manipulate the object using a 7 degrees of freedom torque-controlled robot arm gripper (Franka Emica Robot). An instrumentation platform with an industrial force–torque sensor (HEX24, Wittenstein) was used to obtain ground-truth force measurements and an array of ceramic power resistors (5 W) to simulate temperature variations. The manipulating object was prepared from nylon material via 3D printing (Ultimaker S5, nylon cartridge). The robot control unit and these data acquisition boards are integrated into one system using the ROS. The Data Acquisition Card model PCIe 6228 (National Instruments, USA) and the industrial Force-Torque sensor model ATi Mini85 (ATI, USA) were used to obtain a quantitative analysis of the TENG. The raw sensor values were recorded using analog input from a microcontroller board (Arduino Mega) via a voltage divider circuit. The signal waveforms were recorded by a digital oscilloscope Keysight MSO3054T (Keysight Technologies, USA).

Characterizations: To verify the structural and compositional study of the TENG, the active layer (PVDF film) was characterized using XRD (Mini Flex benchtop X-ray diffractometer, Japan) and FT-IR (Nicolet iS10 FT-IR Spectrometer, Thermo Fisher Scientific Inc., USA). Scanning electron microscopy (ZEISS Crossbeam 540, Germany) was employed to observe the triboelectric layer morphology. An oscilloscope (Tektronix TBS 1000C Series, USA) was used to measure the TENG's open-circuit voltage and short-circuit current waveforms. A full-bridge rectifier (GBJ5010, China) is used to transform alternating current (AC) input into direct current (DC) output. LCR meter (LCR-106X, China) is used to characterize the dielectric properties of the PVDF.

Acknowledgements

This research was supported by the research projects AP14869428 from the Ministry of Science and Higher Education of the Republic of Kazakhstan and 20122022FD4135 from Nazarbayev University.

Conflict of Interest Statement

The authors declare no conflict of interest.

Supporting Information

Supporting Information is available from the Wiley Online Library or from the author.

Keywords

N,N′-poly(methyl methacrylate) (PMMA), robotic tactile sensors, polyvinylidene fluoride (PVDF), quenching, triboelectric nanogenerators (TENGs)

Received: April 30, 2024
Revised: June 10, 2024
Published online: June 14, 2024

[1] S. Hajra, S. Panda, H. Khanberh, V. Vivekananthan, E. Chamanehpour, Y. K. Mishra, H. J. Kim, *Nano Energy* **2023**, *115*, 108729.
[2] N. Turdakyn, A. Medeubayev, I. Abay, D. Adair, G. Kalimuldina, *Materials Today: Proceedings*, Elsevier Ltd, Amsterdam, Netherlands **2021**, pp. 2478–81.
[3] Y. Nurmakanov, G. Kalimuldina, G. Nauryzbayev, D. Adair, Z. Bakenov, *Nanoscale Res. Lett.* **2021**, *16*, 122.

[4] N. K. Das, M. Ravipati, S. Badhulika, *Adv. Funct. Mater.* **2023**, *33*, 2303288.
[5] K. Dong, X. Peng, Z. L. Wang, *Advanced Materials* **2020**, *32*, e1902549.
[6] K. X. Hou, X. Dai, S. P. Zhao, L. B. Huang, C. H. Li, *Nano Energy* **2023**, *116*, 108739.
[7] Q. Zheng, B. Shi, F. Fan, X. Wang, L. Yan, W. Yuan, S. Wang, H. Liu, Z. Li, Z. L. Wang, *Adv. Mater.* **2014**, *26*, 5851.
[8] S. Ye, M. Yan, X. Tan, J. Liang, G. Zeng, H. Wu, B. Song, C. Zhou, Y. Yang, H. Wang, *Appl Catal B* **2019**, *250*, 78.
[9] B. Fatma, S. Gupta, C. Chatterjee, R. Bhunia, V. Verma, A. Garg, *J. Mater. Chem. A Mater.* **2020**, *8*, 15023.
[10] M. M. Rastegardoost, O. A. Tafreshi, Z. Saadatnia, S. Ghaffari-Mosanenzadeh, C. B. Park, H. E. Naguib, *Nano Energy* **2023**, *111*, 108365.
[11] P. Jiao, *Nano Energy* **2021**, *88*, 106227.
[12] P. Martins, A. C. Lopes, S. Lanceros-Mendez, *Progress in Polymer Science* **2014**, *39*, 683.
[13] G. Kalimuldina, N. Turdakyn, I. Abay, A. Medeubayev, A. Nurpeissova, D. Adair, Z. Bakenov, *Sensors* **2020**, *20*(18), 1.
[14] K. Xia, Z. Zhu, H. Zhang, Z. Xu, *Appl. Phys. A Mater. Sci. Process.* **2018**, *124*, 520.
[15] C. Ribeiro, C. M. Costa, D. M. Correia, J. Nunes-Pereira, J. Oliveira, P. Martins, R. Gonçalves, V. F. Cardoso, S. Lanceros-Méndez, *Nat. Protoc.* **2018**, *13*, 681.
[16] M. Jain, Z. Mutlu, J. Mao, J. Zhou, C. Wu, Y. Cao, M. Cakmak, *J. Polym. Sci.* **2023**, *61*, 1132.
[17] N. Turdakyn, Z. Bekezhankyzy, S. Araby, R. Montazami, Z. Bakenov, G. Kalimuldina, *Energy Rep.* **2023**, *10*, 628.
[18] A. Ferri, S. Barrau, R. Bourez, A. Da Costa, M. H. Chambrier, A. Marin, J. Defebvin, J. M. Lefebvre, R. Desfeux, *Compos. Sci. Technol.* **2020**, *186*, 107914.
[19] J. Xia, Z. Zheng, Y. Guo, *Compos. Part A Appl. Sci. Manuf.* **2022**, *157*, 157.
[20] M. Fortunato, D. Cavallini, G. De Bellis, F. Marra, A. Tamburrano, F. Sarto, M. S. Sarto, *Polymers* **2019**, *11*, 1096.
[21] Y. Oka, N. Koizumi, *Bull. Inst. Chem. Res. Kyoto Univ.* **1985**, *63*, 192.
[22] S. J. Kang, Y. J. Park, I. Bae, K. J. Kim, H. C. Kim, S. Bauer, E. L. Thomas, C. Park, *Adv. Funct. Mater.* **2009**, *19*, 2812.
[23] T. Nishiyama, T. Sumihara, E. Sato, H. Horibe, *Polym. J.* **2017**, *49*, 319.
[24] V. Tiwari, G. Srivastava, G., *J. Polym. Res.* **2014**, *21*(587), 1.
[25] S. Yu, Y. Zhang, Z. Yu, J. Zheng, Y. Wang, H. Zhou, *Nano Energy* **2021**, *80*, 105519.
[26] A. De Neef, C. Samuel, G. Stoclet, M. Rguiti, C. Courtois, P. Dubois, J. Soulestin, J. M. Raquez, *Soft Matter* **2018**, *14*, 4591.
[27] A. De Neef, C. Samuel, H. Amorín, G. Stoclet, R. Jiménez, P. Dubois, J. Soulestin, J. M. Raquez, *ACS Appl. Polym. Mater.* **2021**, *2*, 3766.
[28] D. M. Esterly, D. Leo, D. Inman, *Manufacturing of Poly(Vinylidene Fluoride) and Evaluation of its Mechanical Properties*, Virginia Tech, Blacksburg, Virginia **2002**.
[29] Q. Qi, L. Ma, B. Zhao, S. Wang, X. Liu, Y. Lei, C. B. Park, *ACS Appl. Mater. Interfaces* **2020**, *12*, 36568.
[30] C. Zhang, X. Tong, Z. Liu, Y. Zhang, T. Zhang, C. Tang, X. Liu, Q. Chi, *Polymers (Basel)* **2023**, *15*, 2486.
[31] S. Ojha, P. Maity, S. Bera, S. Kumar Si, B. Bhusan Khatua, *Energ. Technol.* **2023**, *11*, 2201086.
[32] C. Mi, Z. Ren, H. Li, S. Yan, X. Sun, *Ind. Eng. Chem. Res.* **2019**, *58*, 7389.
[33] S. Aid, A. Eddhahak, S. Khelladi, Z. Ortega, S. Chaabani, A. Tcharkhtchi, *Polym. Test.* **2019**, *73*, 222.
[34] Y. Zhang, T. Zhang, Z. Huang, J. Yang, *Advanced Science* **2022**, *9*, 2105084.
[35] X. Wang, H. Zhang, L. Dong, X. Han, W. Du, J. Zhai, C. Pan, Z. L. Wang, *Adv. Mater.* **2016**, *28*, 2896.
[36] S. Wang, X. Zhao, X. Yin, J. Yu, B. Ding, *ACS Appl. Mater. Interfaces* **2016**, *8*, 23985.
[37] L. Shi, H. Jin, S. Dong, S. Huang, H. Kuang, H. Xu, J. Chen, W. Xuan, S. Zhang, S. Li, X. Wang, J. Luo, *Nano Energy* **2021**, *80*, 105599.
[38] H. Asai, Y. Terada, K. Nakane, *Polymer (Guildf)* **2022**, *244*, 124650.
[39] D. Lolla, M. Lolla, A. Abutaleb, H. U. Shin, D. H. Reneker, G. G. Chase, *Materials* **2016**, *9*, 671.
[40] L. Lu, W. Ding, J. Liu, B. Yang, *Flexible PVDF based piezoelectric nanogenerators*, Vol. *78*, Elsevier Ltd, Amsterdam, Netherlands **2020**, 105251.
[41] Y. H. Lee, D. H. Kim, Y. Kim, I. Shabbir, M. Li, K. H. Yoo, T. W. Kim, *Nano Energy* **2022**, *102*, 107676.
[42] J. H. Zhang, Z. Zhou, J. Li, B. Shen, T. Zhu, X. Gao, R. Tao, X. Guo, X. Hu, Y. Shi, L. Pan, *ACS Mater. Lett.* **2022**, *4*, 847.
[43] M. M. Rastegardoost, O. A. Tafreshi, Z. Saadatnia, S. Ghaffari-Mosanenzadeh, C. B. Park, H. E. Naguib, *Appl. Mater. Today* **2023**, *30*, 101732.
[44] P. Bai, G. Zhu, Q. Jing, J. Yang, J. Chen, Y. Su, J. Ma, G. Zhang, Z. L. Wang, *Adv. Funct. Mater.* **2014**, *24*, 5807.
[45] Y. Yang, H. Zhang, Z. H. Lin, Y. S. Zhou, Q. Jing, Y. Su, J. Yang, J. Chen, C. Hu, Z. L. Wang, *ACS Nano* **2013**, *7*, 9213.
[46] Z. Zhao, Q. Huang, C. Yan, Y. Liu, X. Zeng, X. Wei, Y. Hu, Z. Zheng, *Nano Energy* **2020**, *70*, 104528.
[47] R. Song, G. Xia, X. Xing, L. He, Q. Zhao, Z. Ma, *J. Colloid Interface Sci.* **2013**, *401*, 50.
[48] J. Wang, H. Wu, Z. Wang, W. He, C. Shan, S. Fu, Y. Du, H. Liu, C. Hu, *Adv. Funct. Mater.* **2022**, *32*, 2203884.